PHOTONICS Research

Interband cascade technology for energy-efficient mid-infrared free-space communication

Pierre Didier,[1,2,*] Hedwig Knötig,[3] Olivier Spitz,[1,4] Laurent Cerutti,[5] Anna Lardschneider,[2] Elie Awwad,[1] Daniel Diaz-Thomas,[5] A. N. Baranov,[4] Robert Weih,[6] Johannes Koeth,[6] Benedikt Schwarz,[3] and Frédéric Grillot[1,7]

[1]LTCI Télécom Paris, Institut Polytechnique de Paris, Palaiseau 91120, France
[2]mirSense, Centre d'intégration NanoInnov, Palaiseau 91120, France
[3]Institute for Solid State Electronics, TU Wien, 1040 Vienna, Austria
[4]Currently with CREOL, College of Optics and Photonics, University of Central Florida, Orlando, Florida 32816, USA
[5]Institut d'Electronique et des Systèmes, Université de Montpellier, CNRS UMR 5214, Montpellier 34000, France
[6]Nanoplus Nanosystems and Technologies GmbH, 97218 Gerbrunn, Germany
[7]Center for High Technology Materials, University of New Mexico, Albuquerque, New Mexico 87106, USA
*Corresponding author: pierre.didier@telecom-paris.fr

Received 26 October 2022; revised 6 December 2022; accepted 20 December 2022; posted 20 December 2022 (Doc. ID 478776); published 0 MONTH 0000

Space-to-ground high-speed transmission is of utmost importance for the development of a worldwide broadband network. Mid-infrared wavelengths offer numerous advantages for building such a system, spanning from low atmospheric attenuation to eye-safe operation and resistance to inclement weather conditions. We demonstrate a full interband cascade system for high-speed transmission around a wavelength of 4.18 µm. The low-power consumption of both the laser and the detector in combination with a large modulation bandwidth and sufficient output power makes this technology ideal for a free-space optical communication application. Our proof-of-concept experiment employs a radio-frequency optimized Fabry–Perot interband cascade laser and an interband cascade infrared photodetector based on a type-II InAs/GaSb superlattice. The bandwidth of the system is evaluated to be around 1.5 GHz. It allows us to achieve data rates of 12 Gbit/s with an on–off keying scheme and 14 Gbit/s with a 4-level pulse amplitude modulation scheme. The quality of the transmission is enhanced by conventional pre- and post-processing in order to be compatible with standard error-code correction.

https://doi.org/10.1364/PR.478776

1. INTRODUCTION

The mid-infrared spectral range is attracting more and more attention because of the potential it holds for various fields like spectroscopy [1] and high-speed free-space transmission [2]. These wavelengths benefit from very low attenuation in the atmosphere and are intrinsically resistant to degraded atmospheric conditions [3]. Various optical sources emitting at mid-infrared wavelengths, in the thermal atmospheric windows 3–5 µm and 8–14 µm, have been developed including optical parametric oscillators [4], supercontinuum generation in fibers and bulk crystals [5–8], and cascaded technology [9]. Historically, many efforts were dedicated to the development of quantum cascade lasers (QCLs), which rely on intersubband transitions in band-engineered quantum wells (QWs). The main advantage of QCLs is the availability of high output power over a wide range of wavelengths and, in addition, a theoretical potential for very high-speed direct modulation due to their ultra-fast transitions [10], which is yet to be confirmed experimentally [11,12]. In contrast, interband cascade technology is based on interband recombination in a broken gap configuration, employing the same cascading principle as QCLs [13]. Technological advantages of interband cascade lasers (ICLs), compared to their QCL counterparts, include the possibility to circumvent the fast phonon scattering losses and the polarization selection rule constraints of the QCL [14] while still achieving sufficiently high output powers of tens of milliwatts [15]. Due to its low lasing threshold, this technology is extremely attractive for many applications requiring low-power consumption. Several aspects of the working principles of ICLs were recently investigated, uncovering limiting factors for their performance like valence intersubband absorption in the active region [16] or relaxation oscillations, which can limit their maximum modulation speed [17]. A key step toward a wider adoption of ICL technology could come from the development of interband cascade (IC) photonic integrated circuits

(PICs), which has seen a growing interest [18–20] since the first demonstrations of ICLs on silicon in 2018 [21,22]. Also, the potential and feasibility of integrating III–V optoelectronics on Si have also been demonstrated for QCLs [23]. Recent works showed the possibility to mitigate a very high dislocation factor, while still keeping the same characteristics as regular ICLs grown on GaSb [22], paving the way for spectroscopic or high-speed chip-based systems at mid-infrared wavelength. The ICL is already a mid-infrared source of choice for molecular spectroscopy [24,25], and recent experimental efforts are poised to extend the capabilities of ICLs to cell ablation in a medical context [26] and to private optical links [27] allowed by mid-infrared hyperchaos [28]. Moreover, simulations based on a semi-classical rate equation model for ICLs are promising for the generation of squeezed states and for quantum-oriented mid-infrared applications [29]. ICLs are also of paramount interest for regular free-space communications. State-of-the-art transmission rates in the 3–5 μm window using cascaded technologies have been demonstrated at 6 Gbit/s with a QCL emitting at 4.65 μm [30]. However, while wavelength conversion can potentially achieve very high data rates, it currently lacks sufficient output power (milliwatts) and requires high power consumption. Conversely, high-speed communication based on ICLs is lagging behind, with a record transmission rate of 300 Mbit/s so far [31]. In the latter, the bandwidth limit is mostly due to the parasitic capacitance of the ICL structure lacking a dedicated high-frequency launcher. Most of the recent articles about mid-infrared communication are also limited by the bandwidth of their mercury cadmium telluride (MCT) detector. This technology is renowned for its high sensitivity, but so far commercial devices slower than the 2.4 GHz bandwidth one can be expected from our radio-frequency (RF)-mounted ICLs [17]. Interestingly, novel mid-infrared photodetectors based on a uni-traveling carrier process showed impressive performances, such as 3 dB bandwidth of tens of GHz and high responsivity up to 600 mA/W [32,33] at 300 K. We decided to investigate the potential of a more mature technology, named interband cascade infrared photodetectors (ICIPs) for free-space communication in a full interband system (ICL and ICIP). Since the first demonstration of this cascaded type of detector employing a type-II superlattice as an absorber in 2010 [34], this promising technology has raised attention from both industry and researchers. Especially, the high-speed behavior has lately moved into the research spotlight with demonstrations of 3 dB cutoff frequencies in the GHz range [35–38]. Moreover, in comparison to a single stage absorber, the cascading principle greatly benefits the detectivity of the ICIP [39]. Compared to the widely used MCT detectors, ICIPs also offer numerous advantages like suppressed Auger recombination, reduced tunneling currents, and high uniformity in their growth [40]. In contrast to their intersubband counterparts, named quantum cascade detectors (QCDs), where 3 dB bandwidths of more than 20 GHz were recently demonstrated [41,42], ICIPs exhibit a narrower electrical bandwidth but a significantly broader spectral response. This allows for a higher degree of flexibility when designing a free-space optical (FSO) communication setup, enabling the use of transmitters over a broader range of wavelengths. In general, ICIPs combine fast detection with high responsivity and a high saturation level when biased [38]. Yet, moderate voltage is required, and the power consumption of the overall IC system is still as low as 1 W at maximum conditions of operation (900 mW for the ICL [17] and 10 mW for the ICIP). In this article, we report on a full interband free-space communication system, allowing for data rates up to 14 Gbit/s when combining a directly modulated ICL emitting around 4.18 μm wavelength and an ICIP. We investigate three different modulation formats: two-level on–off keying (OOK), 4-level pulse amplitude modulation (PAM-4), and 8-level pulse amplitude modulation (PAM-8) [43].

2. EXPERIMENTAL SETUP

We used a 3 mm long and 10 μm wide ridge Fabry–Perot ICL emitting around 4.18 μm as shown in Fig. 1(c). Details about this laser were already presented in a previous article [17], but additional manufacturing information can be found in Appendix A. One can find in Fig. 1(a) the calculated band structure of the W-shape structure of the ICL. This laser was operated at a constant temperature of 20°C. The bias current for the ICL was supplied by a homemade battery source to minimize the current noise in the laser. For a temperature of 20°C and a drive current of 200 mA, a maximum output power of 8 mW can be reached with an operating voltage of 4.5 V. The consumption of the ICL is as low as 0.9 W at maximum output power.

The ICIP was grown by molecular beam epitaxy (MBE) on a compensation-doped GaSb substrate ($n \leq 5 \times 10^{16}$ cm^{-3}) to facilitate reduced free-carrier absorption when illuminating the detector from the substrate side. A 500 nm thick GaSb bottom contact was grown with a doping of $n = 1 \times 10^{18}$ cm^{-3} since the compensation doping lowers the conductivity of the substrate. The bottom contact is followed by three active stages, which are each made of the electron barrier, the active region based on a type-II superlattice, and the hole barrier, in this order, as shown in Fig. 1(b). The absorbers consist of 54 superlattice periods of 1.5 nm GaSb/0.8 nm AlSb/1.5 nm GaSb/2.7 nm InAs, following a design previously reported by Lei *et al.* [40]. The entire active region was left undoped. In order to balance the strain in the structure, 0.15 nm thin InSb layers were grown at the InAs interfaces. This modification leads to a redshift of the cutoff wavelength of about 500 nm compared to the original design. The electron and hole barriers consist of four GaSb/AlSb pairs and eleven InAs/AlSb pairs, respectively. The highly doped ($n = 2 \times 10^{18}$ cm^{-3}) top contact was realized as a lattice matched $InAs_{0.91}Sb_{0.09}$ layer of 50 nm thickness. Transition layers were employed toward the bottom and top contacts to avoid potential barriers at the interface and allow for a smooth transition of the carriers. Circular detector mesas with a diameter of 75 μm were fabricated using reactive ion etching. A Si_3N_4 passivation layer is deposited and selectively removed on top, where the Ti/Au top contact is realized afterward. Forming an Ohmic contact to the n-GaSb bottom contact, Ge/Au/Ni/Au is deposited and thermally annealed. Subsequently, the mesas are mounted on a copper substrate with a slit to facilitate backside illumination and connected to a coplanar waveguide and an end-launch connector.

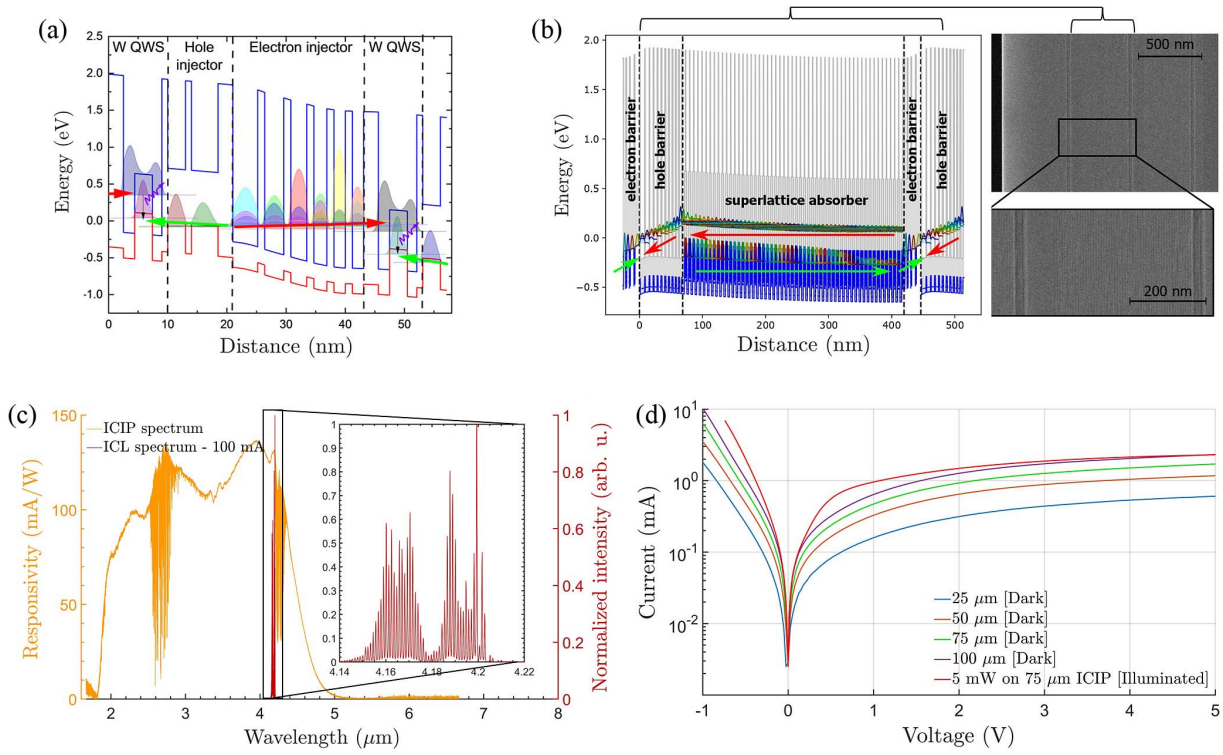

Fig. 1. Characteristics of cascaded interband devices. (a) Calculated band alignment and probability density functions of one stage of the ICL active region for an internal electric field of 80 kV/cm and emission at 4.18 μm [44]. (b) Schematic representation of the band alignment and SEM picture of the heterostructure of the ICIP detector. (c) Measured responsivity of the ICIP under zero bias operation at room temperature (yellow curve) together with the normalized emission spectrum of the ICL at a temperature of 20°C and a drive current of 100 mA (red curve). The detector is well suited for the emission wavelength of the source around 4.18 μm. The inset displays more precisely the emission spectrum of the ICL showing the multimode emission composed by two lobes located left and right of 4.18 μm. (d) Dark current density characterization for four different mesa sizes from 25 μm to 100 μm. With a 4.5 V bias and at 20°C, the 75 μm ICIP shows a dark current of 1.6 mA. When illuminated by the 5 mW ICL beam, the photocurrent is around 2.3 mA.

The responsivity is displayed in Fig. 1(c), exhibiting a rather flat spectral response between 2 and 4.5 μm. At the lasing wavelength of 4.18 μm, the responsivity is evaluated to be around 130 mA/W. As shown in Fig. 1(c), the emission wavelength of the ICL is located near the peak detection of the ICIP. In addition, the intensity–voltage (IV) response of the ICIP as a function of the size of the detector is shown in Fig. 1(d). The 75 μm ICIP exhibits a dark current around 1.6 mA at 4.5 V.

The experimental setup is shown in Fig. 2(a). First, we evaluated the optimal ICL parameters for lowering the non-linearity and achieving the best modulation depth. It is a compromise between the bandwidth, the level of thermal parasitic effects (which both increase with the bias current of the laser), and a sufficient laser output power. Experimentally, the optimum configuration is to bias the ICL at 140 mA for a temperature of 20°C. In order to achieve high-speed electrical modulation of the ICL, we used a Socionext arbitrary waveform generator (AWG), which can provide 120 GS/s, with an analog 3 dB bandwidth of 30 GHz. We generate sequences corresponding to three different modulation schemes: OOK with a non-return to zero (NRZ) format, PAM-4, and PAM-8 [43]. Since 2^{15}-bit long pseudo-random-binary sequences (PRBSs) have been used and they guarantee the occurrence of more combinations of bit sequences than shorter PRBSs, we can study how the transmission system reacts to these different combinations. Moreover, we shaped our signal with a root-raised-cosine (RRC) filter, which decreases the spectral occupation of the transmitted signal with the goal of increasing the data rate of the transmission. The occupied bandwidth of our optical signal can be defined by $B = (1 + \rho)R_s$, in which ρ is the roll-off factor of the filter and R_s is the symbol rate. The roll-off factor satisfies the condition $0 \leq \rho \leq 1$, and an unfiltered signal corresponds to $\rho = 1$, thus to the maximum bandwidth occupancy. The modulated electrical signal from the AWG has an amplitude of $1.5V_{pp}$, which has been amplified upstream with a 10 dB gain D837C SHF differential amplifier. After approximately 2 m free-space propagation, a silicon lens focuses the optical signal on the ICIP. Interestingly, contrary to QCDs, the ICIP detector does not have a polarization requirement for detection. Toward the detection, the ICIP is connected to a Pasternack bias tee. The DC part is used to bias the detector with a Keithley source, and the AC contribution is amplified with a 25 dB gain 826H SHF amplifier before being recorded by a 20 GHz oscilloscope with a sampling rate of 50 GS/s. The resulting DC current of the ICIP when illuminated by a 5 mW laser signal can be found in Fig. 1(d) showing a responsivity in accordance with the announced values of 130 mA/W. After being detected by the oscilloscope, the signal

is processed offline with a MATLAB code. The processing consists in RRC filtering followed by a feed-forward equalizer [45] that will be described below. Then, we compare the recovered bits to the transmitted ones to compute the bit error rate (BER). As shown in Fig. 2(c), one can visualize the superposition of the generated PRBS signal in an OOK configuration in green and the signal received by the ICIP detector in red. In this example, the generated signal is a 10 Gbit/s OOK PRBS pattern. At this data rate, there are strong inter-symbol interferences (ISIs) when you keep alternating a "0"-bit and a "1"-bit, and this shows the frequency limitation of our system, hence justifying the need for equalization algorithm.

3. RESULTS

The bandwidth of the full setup constituted by the amplifiers, laser, and detector was evaluated using a 40 GHz Rohde & Schwarz ZVK vector network analyzer (VNA), in the case where the ICIP detector was used. The VNA is made of an electrical source signal and an electrical receiver. It calculates the input–output relationship between ports in the system as a function of the source signal frequency. In our case, we plugged the source signal of the VNA on the AC input of the laser's bias tee. We plugged the receiver of the VNA at the 25 dB amplified response signal of the ICIP. That gives the amplitude response of our system as a function of the modulating frequency. This response is plotted for four voltage conditions for the ICIP and is quite flat until reaching the cutoff frequency, as shown in Fig. 2(b). By increasing the bias voltage of the detector, one can increase its bandwidth by 1 order of magnitude, from 140 MHz at 0 V to 1.5 GHz at 5 V bias. For the sake of completeness, the response of the full system using a QCD with a 3 dB bandwidth of 20 GHz instead of an ICIP is presented in Appendix C. The 3 dB bandwidth of this mixed

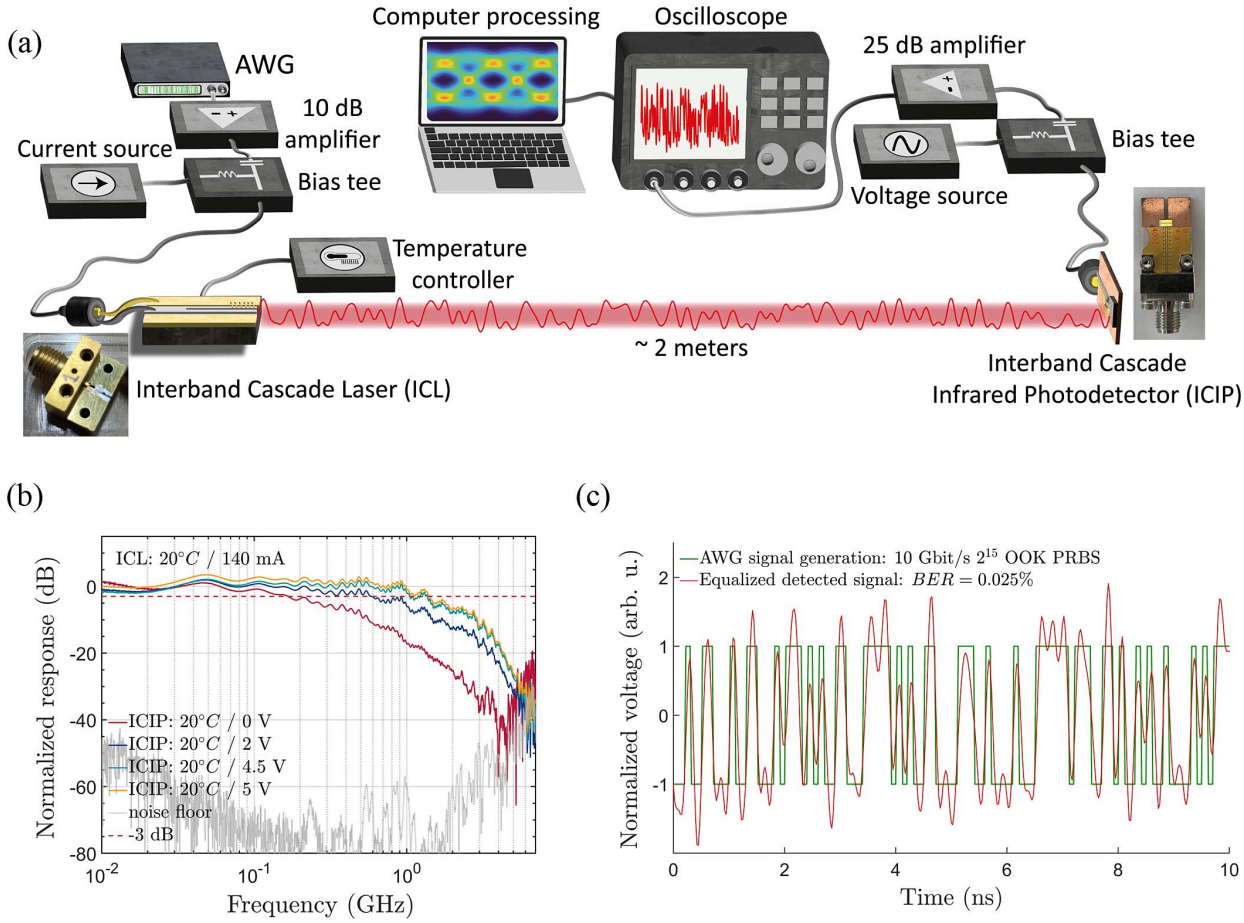

Fig. 2. (a) Experimental setup for the high-speed transmission in the mid-infrared domain with interband cascade devices. At the optimized working condition, the 4.18 μm ICL emits around 5 mW of optical power. We modulate our laser with a 10 dB amplified signal produced by an AWG. The ICIP detects the modulated optical wave and converts it to an electrical signal, which is subsequently fed to a high-speed oscilloscope and then analyzed. Pictures of the devices of interest are shown in insets 1 and 2. The RF-optimized ICL can be seen on the left with its contacts connected to a coplanar waveguide and a 2.92 mm RF-launcher. On the right, the ICIP can be visualized. Short wire bonds are used to connect the contacts to a coplanar waveguide that is attached to an end-launch connector as well. (b) Frequency response of the IC communication system at a pump current of 140 mA for the ICL and with the ICIP biased at, respectively, 0, 2, 4.5, and 5 V. The gray curve represents the noise level in the same configuration when the ICL beam is blocked. For comparison, the frequency response of the system using a 20 GHz 3 dB bandwidth QCD for detection is shown in Appendix C. (c) Time response of the full system recorded by the oscilloscope for a 10 Gbit/s transmission after post-processing (in red) compared to the generated PRBS message (in green). It shows the high-frequency limitation of the system when there is a repeated alternate sequence of "0"-bit and "1"-bit. For the message sequence shown here, the BER is as low as 0.025%.

system is 2.5 GHz, which is the bandwidth of the ICL structure itself because the detector is no longer the limiting device. This 2.5 GHz bandwidth is in very good agreement with our prediction based on the study of the relaxation oscillation frequency [17]. With the ICIP, the system is then limited by the speed of the detector, even at high-voltage bias. As shown in Fig. 1(d), increasing the bias of the detector significantly increases its dark current, which can limit the detection capabilities at low optical power.

After characterizing the setup, we evaluate the capacity of our system to transfer information at different data rates and various modulation schemes. To evaluate the capacity of our system, we mapped a 2^{15}-bit long PRBS to the three aforementioned formats (OOK, PAM-4, and PAM-8). For each transmission, we used an RRC pulse-shaping filter with different roll-off factors in order to reduce the spectral occupation of the transmitted signal. We then chose the roll-off factor minimizing the BER. At the receiver side, we apply a matched filter, which is an RRC filter with the same roll-off factor. Then, the signal is equalized by using fractionally spaced feed-forward equalization (FFE) [45] at a rate of four samples per symbol. The first step of the algorithm learns the coefficients of the channel equalizer by using a least mean squares gradient descent algorithm with a convergence parameter μ, which controls the speed and the accuracy of the learning step. The number of filter coefficients is called n_{tap} and should be large enough to cover all the channel memory. Once the algorithm has converged to achieve an error below a given threshold, the estimated equalizer is applied over the received signal to remove ISI. We evaluated the impact of those parameters on the quality of the transmission in Figs. 3(b) and 3(d). We also plotted the eye diagram in Figs. 3(a) and 3(c), which allows us to represent the capability of our system to distinguish between different bit levels. One can evaluate the presence of non-linearity or systematic errors in the transmitted signal by looking at the distortions of the eye. In addition, a good indicator can be the presence of compression between different bit levels (bit levels are not equally spaced) or a level with an ill-defined eye. The purpose is to optimize the parameters of our equalization in order to reach the lowest BER. The latter has been recovered using the whole traces constituted by 10 million data points sampled at 50 GS/s. In Figs. 3(b) and 3(d), one can see the importance of optimizing the coefficients of the equalization. For the two-level modulation (OOK), μ has an optimal value around 10^{-3} and n_{tap} has to be above 11 to comply with a tabulated threshold BER. Only for particular well-chosen

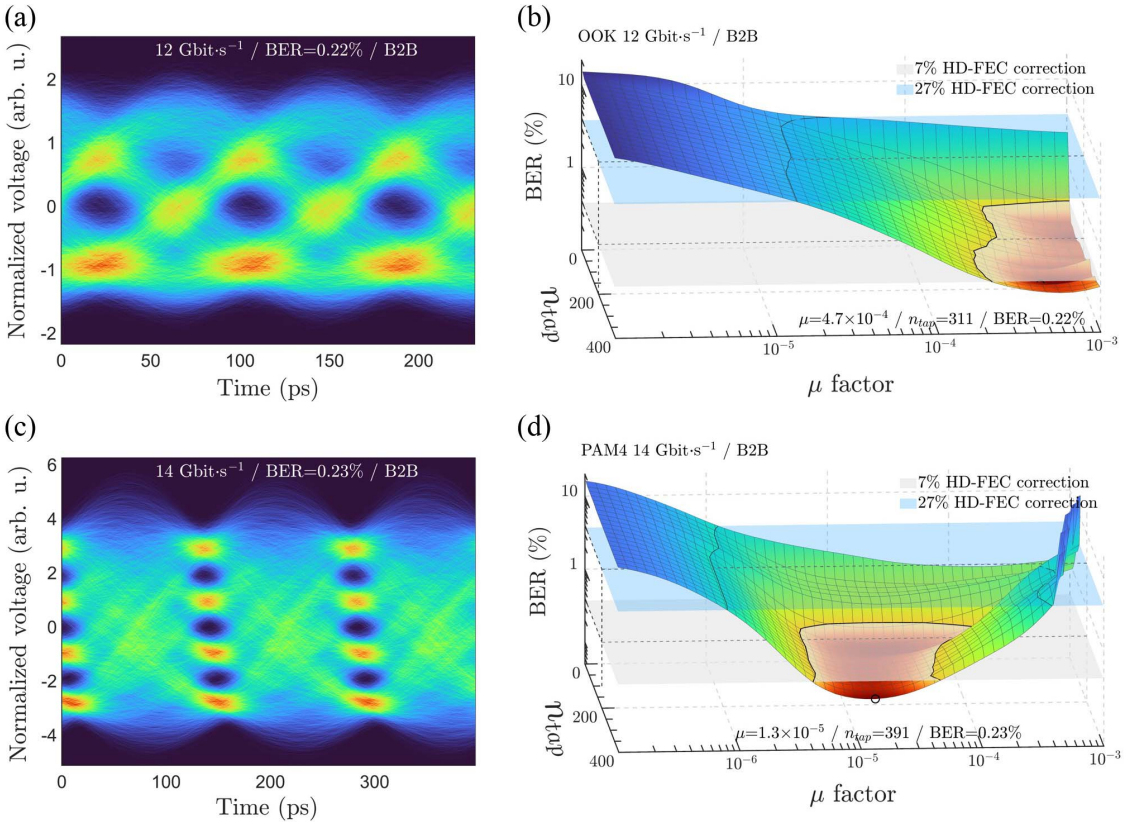

Fig. 3. Eye diagrams of the transmission after a free-space propagation of approximately 2 m for two different modulation formats. An eye diagram represents the overlapping of the recorded signal at a fixed time interval corresponding to an integer multiple of the bit time-length. This tool allows a qualitative analysis of the transmission performance, as an open eye is equivalent to a low error rate because it shows the ability to distinguish the different levels of modulation. (a) OOK format at 12 Gbit/s exhibiting an error rate of 0.22%. (c) PAM-4 format at 14 Gbit/s with an error rate of 0.23%. (b) and (d) show the optimization parameters of FFE equalization in order to achieve the lowest BER. In both cases, there is a particular set of parameters where the equalization allows one to highly optimize the quality of the transmission.

parameters, the equalization process leads to a great improvement in terms of transmission quality. By optimizing these coefficients, we achieve an OOK transmission at a bit rate of 12 Gbit/s with an acceptable BER under 0.38% and 14 Gbit/s with a BER below 4%. The result toward BER satisfying the <4% criterion can be found in Appendix B. Forward error correction (FEC) coding and decoding are used to correct bit errors by introducing redundancy. Hence, an FEC overhead should be taken into account in the dimensioning of the transmission system. For a maximum tolerated pre-FEC BER of 4%, an FEC code with 27% overhead and hard-decision (HD) decoding [46] is assumed to be used to achieve an error-free communication, whereas for a maximum pre-FEC BER of 0.38%, an FEC code with an overhead of only 7% is used. Toward the 4-level format (PAM-4), we achieve a transmission at 14 Gbit/s with a BER of 0.23% and 16 Gbit/s with a BER below 4% (also found in Appendix B). It is relevant to note that the optimal value of the convergence parameter μ has to be lower when considering multi-level modulation formats.

In this work, the 8-level modulation format (PAM-8) was also investigated. Unfortunately, due to noise coming from the amplifier and the detector in our system, we were not able to reach a BER below 0.4%. The parameters were adequately optimized, and the optimum μ factor was again lower compared to lower order multi-level modulation formats as shown in Fig. 4(b). In that case, it is mandatory to use a high n_{tap} value in order to keep a low BER. The presented result in Fig. 4(a) is a 15 Gbit/s transmission associated with a BER of 1.9%. This can be corrected by employing an HD-FEC algorithm using a 27% overhead, which can accommodate a BER up to 4%. It should be noted that using a longer overhead may also introduce more complex decoding associated with higher latency.

We summarize the results of the transmission for the different modulation formats in Fig. 5. We found that good performance is achieved when we have a ρ value of 0.3 for the OOK and PAM-8 modulation formats and a ρ value of 0.4 for the PAM-4 format. This means that we decrease the bandwidth occupation of a modulated optical signal by 35% and 30%, respectively, with the following relationship: $\frac{\Delta B}{\Delta B_{\text{unfiltered}}} = 1 - \frac{1+\rho}{2}$.

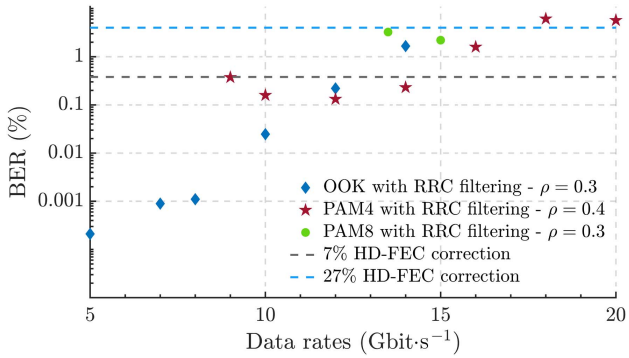

Fig. 5. Evolution of the equalized signal's BER as a function of the data rate for different modulation formats. The dashed lines depict BER limits for 7% HD-FEC (gray) and 27% HD-FEC (cyan), respectively.

It allows us to achieve a BER below the 7% HD-FEC threshold for the OOK and PAM-4 configurations.

4. CONCLUSION

This paper shows the possibility of building a full IC system in one of the transparency windows of the atmosphere with the laser and detector adapted for 4.18 μm wavelength at room temperature. We shaped the signals to be transmitted with an RRC routine before injecting them into the laser in order to optimize the achievable data rate. In addition, the received signal detected by the ICIP was equalized by an FFE algorithm. We performed an optimization of the FFE parameters to minimize the BER. We successfully sent 12 Gbit/s and 14 Gbit/s with the 2-level modulation format (OOK) with a BER suitable for 7% and 27% HD-FEC, respectively. Furthermore, we investigated the possibility of using multi-level modulation formats and saw the effectiveness of equalization to compensate the ISI. The resulting data rates were at 14 Gbit/s and 16 Gbit/s with a 4-level modulation format (PAM-4) with a BER suitable for 7% and 27% HD-FEC, respectively. Hence, moving from a 2-level to a 4-level modulation format improved the achievable data rates by 2 Gbit/s while ensuring comparable

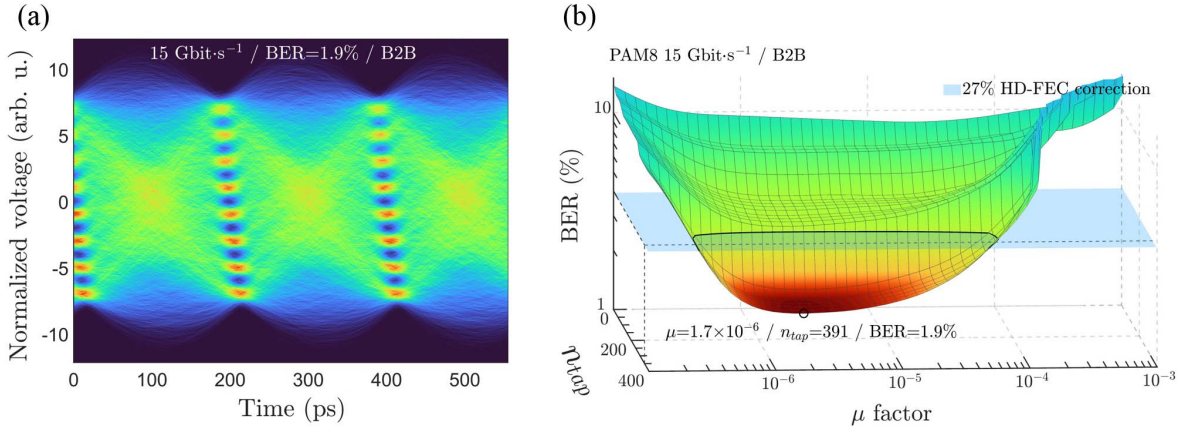

Fig. 4. (a) Eye diagram of the transmission after a free-space propagation of around 2 m for the PAM-8 format at 15 Gbit/s, exhibiting an error rate of 1.9%. (b) Optimization of the FFE equalization parameters in order to achieve the lowest BER.

performances. Finally, we investigated the possibility to use an 8-level modulation format (PAM-8). We successfully implemented a 15 Gbit/s transmission with a BER suitable for 27% HD-FEC correction. Those results are unprecedented with direct modulation of semiconductor lasers in the 3–5 μm window, while benefiting from 10 times lower power consumption of the IC devices compared to their quantum cascade counterparts. In addition, this study assessed that ICIPs are very suitable for FSO communication experiments because of the high electrical bandwidth, wide spectral response, and increased sensitivity. This work is a key step in order to build an energy-efficient system using cascaded interband devices for communication applications. Indeed, such a system can be very interesting in conditions where energy is scarce, like satellites sharing data information or autonomous rovers exploring distant planets. Also, it opens the way for a compact design of this communication apparatus, all integrated on a silicon platform. Still, improvements have to be made in order to increase the speed of both the laser and the detector. This is the subject of ongoing work and will be reported in due course.

APPENDIX A

The ICL was grown by MBE on n-type GaSb substrate and designed for emission at 4.18 μm. The n-cladding is composed of a 740-period AlSb(2.3 Å)/InAs(2.4 Å) superlattice where the first 300 periods were n-doped with Si at 7×10^{17} cm^{-3}. The doping was then reduced to 10^{17} cm^{-3} for the remaining 440 periods. The two 500 nm thick GaSb separate confinement heterostructure (SCH) layers surrounding the seven-stage active region were n-doped with Te at 10^{17} cm^{-3}. The layer sequence of one stage was the following: the "W" Type-II QW is 2.5 nm AlSb/1.9 nm InAs/3.0 nm $Ga_{0.65}In_{0.35}Sb$/1.6 nm InAs/1.0 nm AlSb, the hole injector is 3.0 nm GaSb/1.0 nm AlSb/4.5 nm GaSb/2.5 nm AlSb, and the electron injector is 4.2 nm InAs/1.2 nm AlSb/3.2 nm InAs/1.2 nm AlSb/2.7 nm InAs/1.2 nm AlSb/2.2 nm InAs/1.2 nm AlSb/1.9 nm InAs/1.2 nm AlSb/1.9 nm InAs, where the four InAs layers were n-doped with Si at 4.5×10^{18} cm^{-3} for carrier rebalancing [47]. The upper cladding consisted of 325 periods of AlSb/InAs doped at 10^{17} cm^{-3} and 50 periods doped at 10^{18} cm^{-3}. Finally, a 20 nm thick highly doped InAs contact layer finishes the structure. Then the structure was processed into 10 μm wide ridge lasers by standard photolithography and dry etching using inductively coupled plasma reactive-ion etching (ICP-RIE) with a BCl_3-Cl_2-Ar chemistry down to the middle of the bottom SCH. Electrical insulation and protection were obtained with the Si_3N_4/SiO_2 dielectric deposited by plasma-enhanced chemical vapor deposition (PECVD). Then, Ti–Au was deposited for top contact. The GaSb substrate was thinned down to 150 μm and coated with AuGeNi. The processed wafer was then cleaved into a 3 mm long cavity and soldered epitaxial side down with indium onto RF mounts [17]. Optical facets were left untreated. Figure 1(b) represents the band diagram of one stage of the active region calculated using the Nextnano software [44].

APPENDIX B

We show in Fig. 6 the result toward the transmission satisfying a BER <4% for both the OOK and PAM-4 modulation schemes. In order to achieve error-free communication, the HD-FEC will need a bit overhead of 27% and introduce excessive latency. The latter can be detrimental for high-speed communication.

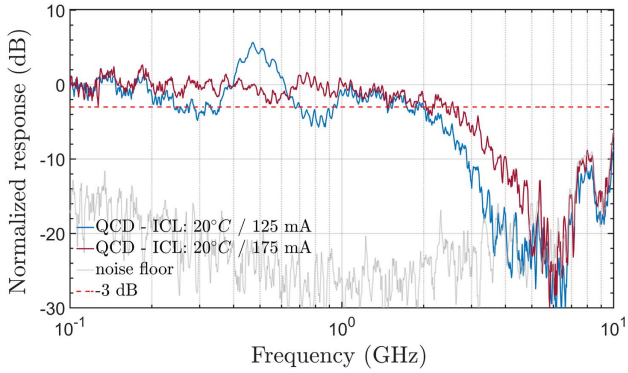

Fig. 7. Frequency response of the system when using a 20 GHz 3 dB bandwidth QCD for detection to replace the ICIP. The whole system now has a 3 dB bandwidth of 2.5 GHz, showing that the full interband configuration with ICL and ICIP is limited by the response of the ICIP.

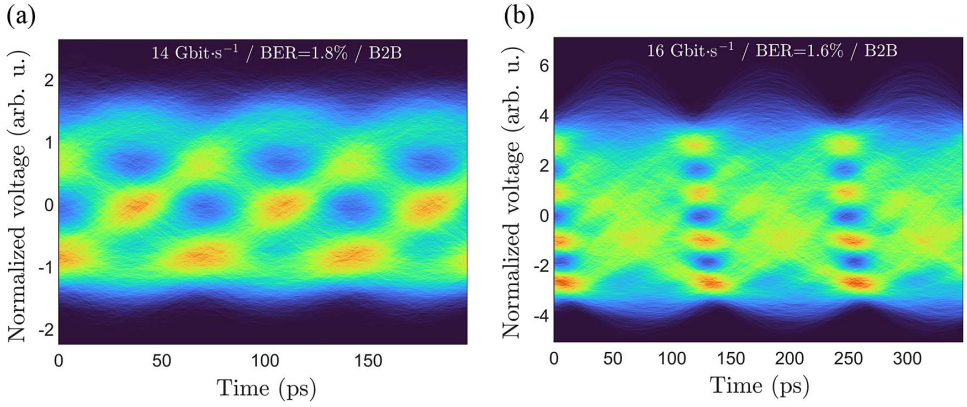

Fig. 6. Eye diagrams of the transmission after a free-space propagation of approximately 2 m for two different modulation formats. (a) OOK format at 14 Gbit/s exhibiting an error rate of 1.8%. (b) PAM-4 format at 16 Gbit/s with an error rate of 1.6%.

APPENDIX C

In order to compare the result with the ICL-ICIP bandwidth measurement, we investigate the optical response of the ICL with a 20 GHz 3 dB bandwidth QCD, whose bandwidth was characterized with a mid-infrared femtosecond oscillator [40]. Since the response of the QCD is flat, we estimated a maximum 3 dB bandwidth of 2.5 GHz for the whole system when the ICL is biased at 175 mA, as shown in Fig. 7, and this is the optimum configuration for high-speed operation of the laser. It is relevant to note that a lower bias current, for instance 125 mA, can unveil the relaxation oscillation frequency of the ICL around 500 MHz, in good agreement with another method already discussed in Ref. [17].

Funding. Agence Nationale de la Recherche (ANR-11-EQPX-0016, ANR-17-ASMA0006); Direction Générale de l'Armement (DGA); European Office of Aerospace Research and Development (FA9550-18-1-7001); European Research Council (853014).

Acknowledgment. The authors thank Prof. Jean-Christophe Cousin (Télécom Paris) and Prof. Wolfgang Elsäßer (Technische Universität Darmstadt) for lending the Vector Network Analyzer and the battery source, respectively.

Disclosures. The authors declare no conflicts of interest.

Data Availability. The data that support the findings of this study are available from the corresponding author upon reasonable request.

REFERENCES AND NOTE

1. J. Haas and B. Mizaikoff, "Advances in mid-infrared spectroscopy for chemical analysis," Annu. Rev. Anal. Chem **9**, 45–68 (2016).
2. S. Blaser, D. Hofstetter, M. Beck, and J. Faist, "Free-space optical data link using Peltier-cooled quantum cascade laser," Electron. Lett. **37**, 778–780 (2001).
3. P. Corrigan, R. Martini, E. A. Whittaker, and C. Bethea, "Quantum cascade lasers and the Kruse model in free space optical communication," Opt. Express **17**, 4355–4359 (2009).
4. B. Cole, L. Goldberg, S. Chinn, L. A. Pomeranz, K. T. Zawilski, P. G. Schunemann, and J. McCarthy, "Compact and efficient mid-IR OPO source pumped by a passively *Q*-switched Tm:YAP laser," Opt. Lett. **43**, 1099–1102 (2018).
5. J. H. Price, T. M. Monro, H. Ebendorff-Heidepriem, F. Poletti, P. Horak, V. Finazzi, J. Y. Leong, P. Petropoulos, J. C. Flanagan, G. Brambilla, X. Feng, and D. Richardson, "Mid-IR supercontinuum generation from nonsilica microstructured optical fibers," IEEE J. Sel. Top. Quantum Electron. **13**, 738–749 (2007).
6. P. Domachuk, N. Wolchover, M. Cronin-Golomb, A. Wang, A. K. George, C. Cordeiro, J. C. Knight, and F. Omenetto, "Over 4000 nm bandwidth of mid-IR supercontinuum generation in sub-centimeter segments of highly nonlinear tellurite PCFs," Opt. Express **16**, 7161–7168 (2008).
7. F. Silva, D. Austin, A. Thai, M. Baudisch, M. Hemmer, D. Faccio, A. Couairon, and J. Biegert, "Multi-octave supercontinuum generation from mid-infrared filamentation in a bulk crystal," Nat. Commun. **3**, 807 (2012).
8. C. R. Petersen, U. Møller, I. Kubat, B. Zhou, S. Dupont, J. Ramsay, T. Benson, S. Sujecki, N. Abdel-Moneim, Z. Tang, D. Furniss, A. Seddon, and O. Bang, "Mid-infrared supercontinuum covering the 1.4–13.3 μm molecular fingerprint region using ultra-high NA chalcogenide step-index fibre," Nat. Photonics **8**, 830–834 (2014).
9. J. Faist, F. Capasso, D. L. Sivco, C. Sirtori, A. L. Hutchinson, and A. Y. Cho, "Quantum cascade laser," Science **264**, 553–556 (1994).
10. C. Wang, F. Grillot, V. Kovanis, and J. Even, "Rate equation analysis of injection-locked quantum cascade lasers," J. Appl. Phys. **113**, 063104 (2013).
11. A. Calvar, M. I. Amanti, M. Renaudat St-Jean, S. Barbieri, A. Bismuto, E. Gini, M. Beck, J. Faist, and C. Sirtori, "High frequency modulation of mid-infrared quantum cascade lasers embedded into microstrip line," Appl. Phys. Lett. **102**, 181114 (2013).
12. B. Hinkov, A. Hugi, M. Beck, and J. Faist, "Rf-modulation of mid-infrared distributed feedback quantum cascade lasers," Opt. Express **24**, 3294–3312 (2016).
13. R. Q. Yang, "Infrared laser based on intersubband transitions in quantum wells," Superlattices Microstruct. **17**, 77–83 (1995).
14. R. Yang, "Mid-infrared interband cascade lasers based on type-II heterostructures," Microelectron. J. **30**, 1043–1056 (1999).
15. I. Vurgaftman, W. W. Bewley, C. L. Canedy, C. S. Kim, M. Kim, C. D. Merritt, J. Abell, and J. R. Meyer, "Interband cascade lasers with low threshold powers and high output powers," IEEE J. Sel. Top. Quantum Electron. **19**, 1200210 (2013).
16. H. Knötig, J. Nauschütz, N. Opačak, S. Höfling, J. Koeth, R. Weih, and B. Schwarz, "Mitigating valence intersubband absorption in interband cascade lasers," Laser Photon. Rev. **16**, 2200156 (2022).
17. P. Didier, O. Spitz, L. Cerutti, D. Diaz-Thomas, A. Baranov, M. Carras, and F. Grillot, "Relative intensity noise and intrinsic properties of RF mounted interband cascade laser," Appl. Phys. Lett. **119**, 171107 (2021).
18. Y. Li, Z. Song, Z. Li, G. Sun, C. S. Tan, W. Fan, and Q. J. Wang, "Theoretical design of mid-infrared interband cascade lasers in SiGeSn system," New J. Phys. **22**, 083061 (2020).
19. J. R. Meyer, C. S. Kim, M. Kim, C. L. Canedy, C. D. Merritt, W. W. Bewley, and I. Vurgaftman, "Interband cascade photonic integrated circuits on native III-V chip," Sensors **21**, 599 (2021).
20. H. Lin, C. S. Kim, L. Li, M. Kim, W. W. Bewley, C. D. Merritt, C. L. Canedy, I. Vurgaftman, A. Agarwal, K. Richardson, J. Hu, and J. R. Meyer, "Monolithic chalcogenide glass waveguide integrated interband cascaded laser," Opt. Mater. Express **11**, 2869–2876 (2021).
21. A. Spott, E. J. Stanton, A. Torres, M. L. Davenport, C. L. Canedy, I. Vurgaftman, M. Kim, C. S. Kim, C. D. Merritt, W. W. Bewley, J. R. Meyer, and J. E. Bowers, "Interband cascade laser on silicon," Optica **5**, 996–1005 (2018).
22. L. Cerutti, D. A. D. Thomas, J.-B. Rodriguez, M. R. Calvo, G. Patriarche, A. N. Baranov, and E. Tournié, "Quantum well interband semiconductor lasers highly tolerant to dislocations," Optica **8**, 1397–1402 (2021).
23. H. Nguyen-Van, A. N. Baranov, Z. Loghmari, L. Cerutti, J.-B. Rodriguez, J. Tournet, G. Narcy, G. Boissier, G. Patriarche, M. Bahriz, E. Tournié, and R. Teissier, "Quantum cascade lasers grown on silicon," Sci. Rep. **8**, 7206 (2018).
24. J. Scheuermann, P. Kluczynski, K. Siembab, M. Straszewski, J. Kaczmarek, R. Weih, M. Fischer, J. Koeth, A. Schade, and S. Höfling, "Interband cascade laser arrays for simultaneous and selective analysis of C1–C5 hydrocarbons in petrochemical industry," Appl. Spectrosc. **75**, 336–342 (2021).
25. G. Yan, L. Zhang, C. Zheng, M. Zhang, K. Zheng, F. Song, W. Ye, Y. Zhang, Y. Wang, and F. K. Tittel, "Mobile vehicle measurement of urban atmospheric CH_4/C_2H_6 using a midinfrared dual-gas sensor system based on interband cascade laser absorption spectroscopy," IEEE Trans. Instrum. Meas. **71**, 9509411 (2022).
26. E. Larson, M. Hines, M. Tanas, B. Miller, M. Coleman, and F. Toor, "Mid-infrared absorption by soft tissue sarcoma and cell ablation utilizing a mid-infrared interband cascade laser," J. Biomed. Opt. **26**, 043012 (2021).
27. O. Spitz, A. Herdt, J. Wu, G. Maisons, M. Carras, C.-W. Wong, W. Elsäßer, and F. Grillot, "Private communication with quantum cascade laser photonic chaos," Nat. Commun. **12**, 3327 (2021).
28. Y. Deng, Z.-F. Fan, B.-B. Zhao, X.-G. Wang, S. Zhao, J. Wu, F. Grillot, and C. Wang, "Mid-infrared hyperchaos of interband cascade lasers," Light Sci. Appl. **11**, 7 (2022).

29. S. Zhao and F. Grillot, "Modeling of amplitude squeezing in a pump-noise-suppressed interband cascade laser," IEEE Photon. J. **14**, 1924208 (2022).
30. K. Zou, K. Pang, H. Song, J. Fan, Z. Zhao, H. Song, R. Zhang, H. Zhou, A. Minoofar, C. Liu, X. Su, N. Hu, A. McClung, M. Torfeh, A. Arbabi, M. Tur, and A. E. Willner, "High-capacity free-space optical communications using wavelength-and mode-division-multiplexing in the mid-infrared region," Nat. Commun. **13**, 7662 (2022).
31. O. Spitz, P. Didier, L. Durupt, D. A. Daz-Thomas, A. N. Baranov, L. Cerutti, and F. Grillot, "Free-space communication with directly modulated mid-infrared quantum cascade devices," IEEE J. Sel. Top. Quantum Electron. **28**, 1200109 (2021).
32. J. Huang, Z. Xie, Y. Chen, J. E. Bowers, and B. Chen, "High speed mid-wave infrared uni-traveling carrier photodetector," IEEE J. Quantum Electron. **56**, 4000807 (2020).
33. J. Huang, Z. Shen, Z. Wang, Z. Zhou, Z. Wang, B. Peng, W. Liu, Y. Chen, and B. Chen, "High-speed mid-wave infrared uni-traveling carrier photodetector based on InAs/InAsSb type-II superlattice," IEEE Electron Device Lett. **43**, 745–748 (2022).
34. R. Q. Yang, Z. Tian, Z. Cai, J. F. Klem, M. B. Johnson, and H. C. Liu, "Interband-cascade infrared photodetectors with superlattice absorbers," J. Appl. Phys. **107**, 054514 (2010).
35. H. Lotfi, L. Li, L. Lei, H. Ye, S. Shazzad Rassel, Y. Jiang, R. Q. Yang, T. D. Mishima, M. B. Santos, J. A. Gupta, and M. B. Johnson, "High-frequency operation of a mid-infrared interband cascade system at room temperature," Appl. Phys. Lett. **108**, 201101 (2016).
36. Y. Chen, X. Chai, Z. Xie, Z. Deng, N. Zhang, Y. Zhou, Z. Xu, J. Chen, and B. Chen, "High-speed mid-infrared interband cascade photodetector based on InAs/GaAsSb type-II superlattice," J. Lightwave Technol. **38**, 939–945 (2020).
37. Z. Xie, J. Huang, X. Chai, Z. Deng, Y. Chen, Q. Lu, Z. Xu, J. Chen, Y. Zhou, and B. Chen, "High-speed mid-wave infrared interband cascade photodetector at room temperature," Opt. Express **28**, 36915–36923 (2020).
38. L. M. Krüger, J. Hillbrand, J. Heidrich, M. Beiser, R. Weih, J. Koeth, C. R. Phillips, B. Schwarz, G. Strasser, and U. Keller, "High-speed interband cascade infrared photodetectors: photo-response saturation by a femtosecond oscillator," Opt. Express **29**, 14087–14100 (2021).
39. R. Q. Yang and R. T. Hinkey, "Ultimate detectivity of multiple-stage interband cascade infrared photodetectors," Appl. Phys. Lett. **118**, 241101 (2021).
40. L. Lei, L. Li, H. Lotfi, H. Ye, R. Q. Yang, T. D. Mishima, M. B. Santos, and M. B. Johnson, "Midwavelength interband cascade infrared photodetectors with superlattice absorbers and gain," Opt. Eng. **57**, 011006 (2017).
41. J. Hillbrand, L. M. Krüger, S. D. Cin, H. Knötig, J. Heidrich, A. M. Andrews, G. Strasser, U. Keller, and B. Schwarz, "High-speed quantum cascade detector characterized with a mid-infrared femtosecond oscillator," Opt. Express **29**, 5774–5781 (2021).
42. G. Quinchard, C. Mismer, M. Hakl, J. Pereira, Q. Lin, S. Lepillet, V. Trinité, A. Evirgen, E. Peytavit, J. Reverchon, J. F. Lampin, S. Barbieri, and A. Delga, "High speed, antenna-enhanced 10.3 μm quantum cascade detector," Appl. Phys. Lett. **120**, 091108 (2022).
43. J. G. Proakis and M. Salehi, *Digital Communications* (McGraw-Hill, 2008), Chap. 3.
44. See https://www.nextnano.de/ for obtaining the nextnano executables and related publications.
45. S. Haykin, *Digital Communications* (Wiley, 1988), Chap. 9.
46. F. Chang, K. Onohara, and T. Mizuochi, "Forward error correction for 100 G transport networks," IEEE Commun. Mag. **48**, S48–S55 (2010).
47. I. Vurgaftman, W. Bewley, C. Canedy, C. Kim, M. Kim, C. Merritt, J. Abell, J. Lindle, and J. Meyer, "Rebalancing of internally generated carriers for mid-infrared interband cascade lasers with very low power consumption," Nat. Commun. **2**, 585 (2011).